ADVANCED MATERIALS INTERFACES
Open Access
www.advmatinterfaces.de

Region-Selective Growth of Cu_2O Shell on Gold Nanoprisms

*Ziyoda Ganieva, Dávid Kovács, Zoltán Osváth, Dániel Zámbó, and András Deák**

Structural control in metal/semiconductor multicomponent nanoparticles can lead to advanced functional properties, as optoelectronic processes and accessibility (e.g., by charge carriers or molecules) of the different components can be simultaneously tailored. In this study, the impact of surface-adsorbed molecules (5-amino-2-mercaptobenzimidazole - AMBI) on the wet-chemical deposition of cuprous oxide (Cu_2O) shells on gold nanoprisms is investigated. It is shown that the otherwise excellent compatibility between gold and Cu_2O, and hence the shell deposition, is profoundly influenced by the presence of AMBI. The time evolution of the optical and structural properties during the shell growth indicates that the inherent Volmer-Weber characteristic of the Cu_2O deposition process gets greatly amplified by the surface adsorption of AMBI. Measurements performed on individual nanoparticles show that this originates in the inhomogeneous, multi-patch coverage of the particle surface. Under optimized synthetic conditions, the tips of the nanoprisms are effectively protected from Cu_2O overgrowth and are left bare.

1. Introduction

Chemical surface modification determined bottom-up strategies for tailoring the structure of metal/semiconductor nanoparticles offers a promising route for the large-scale preparation of functional nanoparticles. The charge generation and separation processes in metal/semiconductor nanoparticles upon photon absorption can enable their use in energy harvesting and catalytic processes, which can be further improved by controlling the structure of nanoparticles.[1] Nanosized heteroparticles prepared from gold and cuprous oxide (Cu_2O) combine the excellent stability of the plasmonic metal with the earth abundance of the direct band-gap, p-type oxide semiconductor, and show excellent compatibility during wet-chemical growth processes despite their ≈5% lattice mismatch.[2–4] Various gold/cuprous oxide (Au/Cu_2O) heteroparticles have been prepared earlier, incorporating nanosized gold spheres, rods, octahedra, or prisms in ⟨100⟩ or ⟨111⟩ terminated Cu_2O particles.[5–9] Regarding the charge carrier separation dependent catalytic properties, the simultaneous access to the metal and semiconductor phases (e.g., by well-defined, surface-grown gold domains on the Cu_2O nanoparticles) is beneficial compared to an enclosed, core/shell-like structure.[4] This can also be achieved by exposing the metal particle, realizing a partial shell coverage,[7] an approach that has been successfully demonstrated to be feasible for the electrocatalytic reduction of CO_2.[10] At the heart of this wet-chemical partial Cu_2O shell formation lies the surface energy modulation of the gold core particles by means of controlled molecular surface modification. The surface modification can reduce the otherwise excellent compatibility between gold and Cu_2O and can block the semiconductor growth region-selectively. A prototypical molecule that can effectively modulate the surface energy of the gold particles is 5-amino-2-mercaptobenzimidazole (AMBI),[11] which can be used for growing metal patches on metal nanoparticles,[12–15] but also successfully employed to partially expose the metal core of gold/Cu_2O core/shell particles.[7,10] The surface adsorbed AMBI molecules promote the island type (Volmer-Weber) coating growth,[16] and can lead to a large structural diversity upon additional material growth.[10,17] The exact impact of the surface-attached, shell-structure-determining molecules remains elusive, primarily due to the limited accessibility to primary data regarding their exact surface distribution on the metal nanoparticles. Nevertheless, it is widely accepted that even for thiol molecules, such as AMBI, the surface accumulation during a wet-chemical process will be more pronounced in the highly curved regions of the metal nanoparticles (tips and edges).[18,19]

In this work, we investigate the impact of AMBI on the Cu_2O shell growth on gold nanoprisms. In an earlier work, it was already demonstrated that despite the geometrical mismatch between the prism-shaped gold core and the preferred cubic or octahedral structure of Cu_2O, a core/shell structure can be achieved for relatively thick shells, with the important notion that shell growth is more pronounced in the tip region of the prisms.[20]

Z. Ganieva, D. Kovács, Z. Osváth, D. Zámbó, A. Deák
HUN-REN Centre for Energy Research
Budapest H-1121, Hungary
E-mail: andras.deak@ek.hun-ren.hu

Z. Ganieva
Institute of Chemistry
University of Pécs
Pécs H-7624, Hungary

D. Kovács
Department of Physical Chemistry and Materials Science
Budapest University of Technology and Economics
Budapest H-1111, Hungary

The ORCID identification number(s) for the author(s) of this article can be found under https://doi.org/10.1002/admi.202500512

DOI: 10.1002/admi.202500512

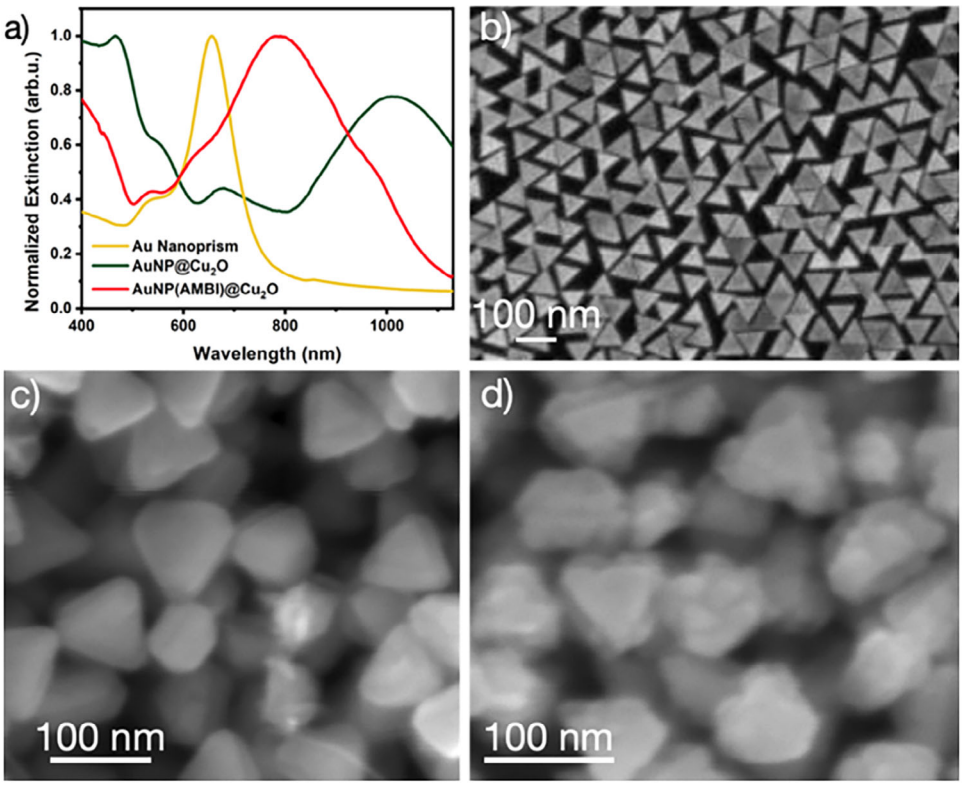

Figure 1. Extinction spectra a) and SEM image of the purified gold nanoprisms b), Cu_2O shell grown without c) and with AMBI d).

Here we show that under proper conditions, this tip-preferred growth of the Cu_2O shell can be suppressed, leading to a partial, tip-exposed core/shell structure. While in situ optical spectroscopy provides a convenient way to monitor both the ligand binding and Cu_2O shell growth, time-dependent electron microscopy reveals both the uncoated character of the prism tips and the island-type growth of the Cu_2O patches at the prism surface when AMBI is present at appropriate surface coverage. Scanning probe microscopy measurements performed on individual nanoparticles suggest that the inhomogeneous surface distribution of the molecules is responsible for the observed growth process.

2. Results and Discussion

The synthesized and purified nanoprisms have an edge length of 75±6 nm, and their dipolar plasmon peak is located at 656 nm (**Figure 1**). The synthetic conditions for the Cu_2O shell growth were modified compared to earlier results,[20] so that a relatively thin shell is obtained, making it easier to capture any impact of AMBI on the shell deposition in later experiments. The main factors investigated were the concentration of nanoprism and copper precursor ($CuCl_2$) (see Figures S1 and S2, Supporting Information for details). The most uniform, shape-conform Cu_2O shell was obtained at 63 μM final Au^0 concentration, and the lowest copper precursor concentration that resulted in a homogeneous shell was found to be 150 μM. Further reduction of the copper ion concentration apparently interferes with the reaction kinetics, abruptly deteriorating the quality of the particles due to overoxidation and random partial coverage. The core/shell particle grown under these optimized conditions had a conformal Cu_2O shell (Figure 1c) with a thickness of ca. 20 nm.

To determine the amount of AMBI that is necessary to modulate the shell growth without fundamentally altering the growth process, its concentration was varied in the 1–190.5 μM range (see Figures S3 and S4, Supporting Information for details), with 1 μM corresponding to ca. 24 % calculated monolayer coverage (Figure S5, Supporting Information), estimating 0.25 nm^2/molecule for AMBI.[21] The resulting Au/Cu_2O particles clearly show that the shell growth is disturbed by the presence of AMBI, but the developing shell has a complex 3D shape, and it is difficult to conceive the actual structure based only on the SEM images. Nevertheless, above 10 μM AMBI concentration cubic cubic-shaped Cu_2O domains appear, and applying an even larger excess completely prevents the shell deposition, and the formation of large cubic Cu_2O particles is observed. This is in accordance with the dominant morphology developing under these conditions for the homogeneous nucleation of Cu_2O particles.[22] At 1 μM AMBI concentration, a relatively homogeneous particle coating can be observed with granular patches on the particles (Figure 1d). Its extinction spectrum is less blueshifted compared to the neat Cu_2O coating grown under otherwise identical conditions (Figure 1a).

To be able to attribute the structural and optical differences observed for the AMBI-treated particles compared to the neat core/shell particles, optical spectroscopy was employed to confirm AMBI adsorption on the nanoprisms (**Figure 2a**). Even at room temperature, a small, but clear 1.5 nm redshift of the

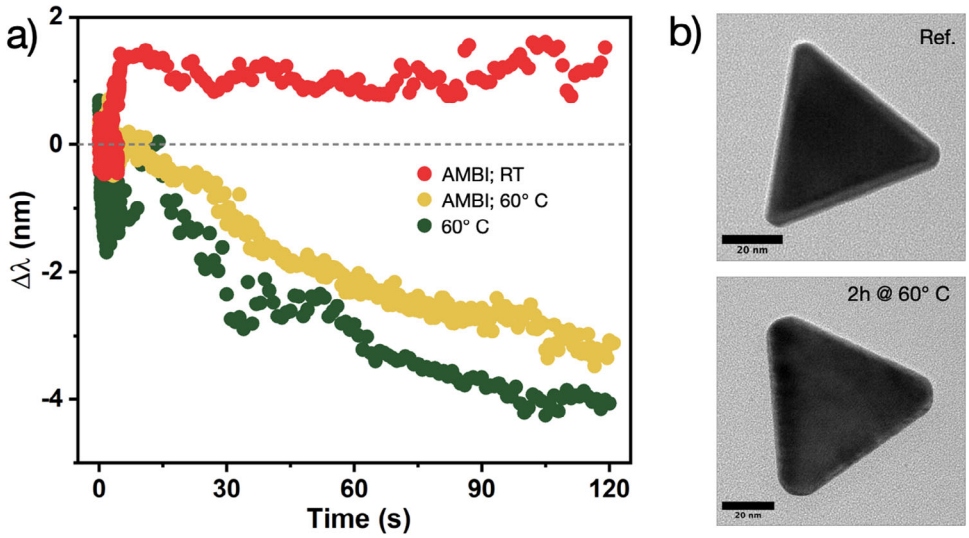

Figure 2. Time-dependent spectroscopy data obtained for the AMBI treatment a), and TEM images demonstrating a slight rounding of the tips after the 2 h-long heat treatment at 60 °C b).

prisms' main dipolar plasmon peak can be detected, which is especially pronounced in the first few minutes due to the strong affinity of AMBI toward the gold surface.[23] Earlier results indicated that small thiol molecule adsorption on gold nanoparticles (rods or prisms) generally results in a blueshift due to the displacement of the native cetyltrimethylammonium (CTA^+) capping layer inherently present on these particles' surface, leading to reduction of the effective refractive index in the optical near field region, while accumulation of larger (macro)molecules is expected to induce a redshift.[24,25] The observed redshift for the smaller-sized AMBI in the present case can presumably be attributed to a higher packing density at the interface, especially at the tips and edges, since the dipolar plasmon mode of the prisms is a tip/edge mode, or the sustained presence of CTA^+ over the adsorbed AMBI molecules.[26,27]

The actual ligand exchange prior to Cu_2O shell growth is performed at 60 °C to promote ordering of the AMBI molecules,[12,28] under which conditions blueshift over the whole investigated time range is found. It has to be noted that for the pristine Au prisms, an even larger blueshift is observed. This latter finding might be explained by the slight reshaping of the particles, which is evidenced by the tip-rounding observed in TEM after 2 h (Figure 2b). Nevertheless, at 60 °C the same redshift due to AMBI is observed compared to the 60 °C reference (Figure S6, Supporting Information).

The Cu_2O shell growth has also been followed spectroscopically, extracting the wavelength position change of the main dipolar plasmon peak (**Figure 3**). A significant redshift and broadening of the main dipolar resonance peak for both of the samples is observed (without AMBI and AMBI treated at 60 °C for 2 h, Figure 3a,b). This is the result of the Cu_2O shell growth, which also results in the appearance of higher-order modes ≈650 nm.[20] As observed for the extracted main dipolar resonance wavelength change, the shell deposition is a quick process, and most of the redshift takes place in the 1 min, especially for the untreated sample (Figure 3c). For the AMBI-treated sample the initial phase of the shell deposition shows an inhibited growth with a prolonged redshift. This implies that for the two cases, a different surface energy landscape is created by AMBI molecules, and the molecules might prevent Cu_2O deposition in particle regions (tips/edges), whose dielectric environment determines the resonance energy. Additionally, these initial spectral differences remain at later stages, and the final redshift values differ significantly (ca. 225 and 130 nm for the untreated and AMBI-treated samples, respectively, Figure 3d). Hence, the observed spectroscopic signatures already indicate a different coverage or structure of the Cu_2O shell.

The time-dependent TEM investigations reveal the cause of the spectroscopically observed differences (**Figure 4**). For the untreated prisms (Figure 4a), a uniform build-up of the coating is observed in general, starting from the early stages with the formation of a few nm sized grains. As early as at 45 s, extended Moiré patterns can be observed over the plane of the nanoprisms, indicating the pronounced presence of the Cu_2O phase, which is in intimate contact with the gold prisms' ⟨111⟩ facets. The homogeneous extension of the deposited material can be observed along the particle perimeter, leading to a neat core/shell structure by the end of the growth process. This observation, together with the SEM images, confirms the shape-conformal wrapping of the pristine prisms by the Cu_2O. For the AMBI-treated sample, a strikingly different shell growth is observed (Figure 4b). Already at the very start of the process (15 s) smaller amount of material is present, which agrees with the spectroscopically derived delay of the plasmon redshift. More importantly, already for the first sample investigated, a low coverage of the prisms' face can be seen, and Moiré fringes of small, patch-like regions can be observed. Hence, the formation of small Cu_2O islands can be suspected. At 45 s into the growth process, these Moiré-patterns get more pronounced and extended, indicating a more complete coverage of the prisms' lateral sites. On the edges, however, larger blob-like domains are developed, and the tips remain uncoated. At later stages, the shell in the edge region grows more homogeneous, but this blob-like structure can still be inferred. At the same time, the tips of the prisms are not overcoated by Cu_2O even

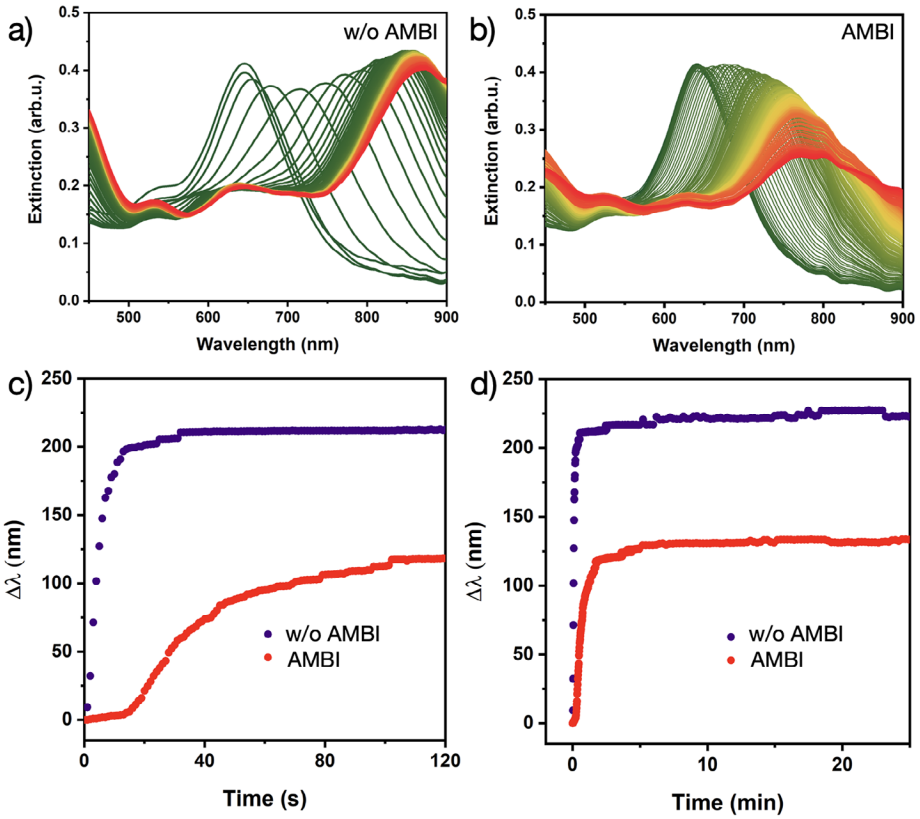

Figure 3. Extinction spectra recorded during the Cu_2O shell growth for the untreated a) and AMBI-treated (1 μM) nanoprisms b). Extracted wavelength shift of the main dipolar plasmon peak in the first 2 min c) and over the entire reaction time d).

at the end of the process (30 min). The above findings suggest that for the AMBI-treated sample the Cu_2O growth is initiated at unprotected surface sites of the prisms, which extend over time, and that AMBI might be present at larger surface concentration at the edge and (especially) at the tips of the prisms.

It has to be noted that the 60 °C heat treatment is necessary to obtain the exposed prism tips. When the AMBI treatment is performed instead of 60 °C at room temperature, the shell morphology resembles the pristine system (without AMBI treatment) (Figure S7a, Supporting Information). Similarly, the plasmon

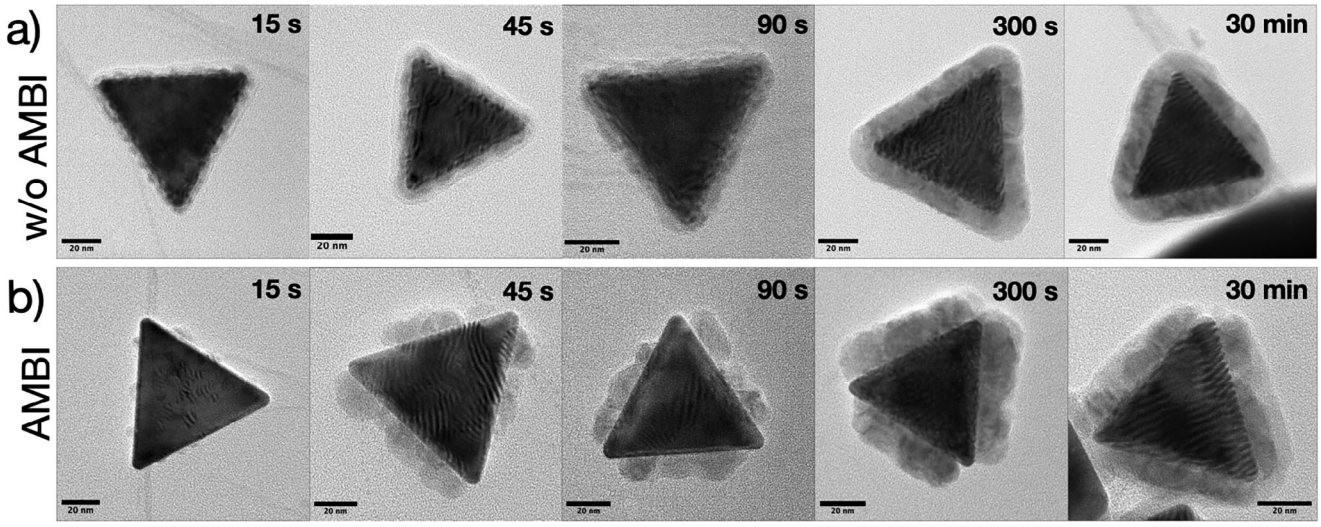

Figure 4. TEM images obtained at different time instances of the Cu_2O shell growth process for the reference (without AMBI) a) and the AMBI surface-modified nanoprisms b). Scale bars: 20 nm.

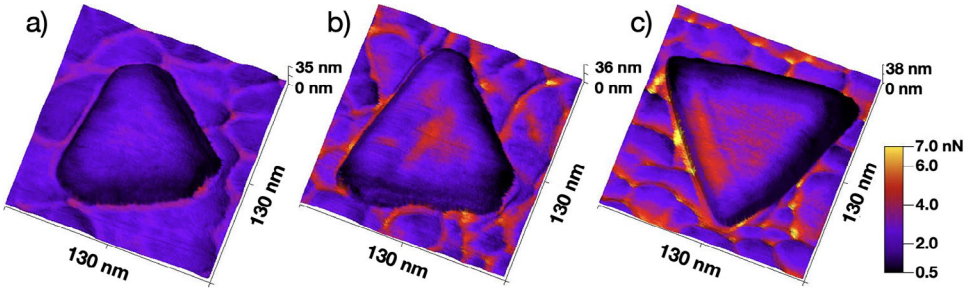

Figure 5. Scanning probe microscopy measurements of the nanoprisms, the color-coded adhesion force map overlain with the topography: no AMBI treatment a) and surface modification at 1 μM b), and 190.5 μM AMBI c).

shift derived from the spectra for the room temperature system indicate that despite a slightly slower deposition rate in the early stage of the growth, the same final redshift values are obtained at the end of the growth process as for the particle without surface modification (Figure S7b,c, Supporting Information). It can be inferred that the elevated temperature is indeed crucial for the development of molecular patches at the particle surface. Without it, a rather statistical distribution of the AMBI molecules can be expected, which is not able to spatially modulate shell growth, and it can grow into a uniform coating resembling that of the pristine system.

To further investigate the role of eventual AMBI patches in directing the Cu_2O shell growth, peak-force scanning probe microscopy measurements have been performed on individual nanoprisms right after the AMBI treatment (without Cu_2O shell growth). It has to be emphasized that a great advantage of the prism-shaped particles is that they feature a relatively large, flat surface region, allowing to measure adhesion force inhomogeneities in these regions (tip/edge regions are not suitable due to edge effects). **Figure 5** shows the combined topography images of individual nanoprisms with the color-coded adhesion force map overlay.

The lowest and highest AMBI loadings are represented by particles that were either not AMBI treated at all (Figure 5a) or were exposed to such a high AMBI concentration (190.5 μM) (Figure 5c), that was shown to entirely prevent Cu_2O shell growth and resulted instead in the homogeneous nucleation of cubic shaped Cu_2O particles (Figure S4, Supporting Information). It can be observed that the AMBI coverage leads to an increase in the adhesion in general, but there is an important difference in the distribution of the adhesion at the planar regions of the prisms. For the lowest and highest investigated loadings, the force maps indicate a rather homogeneous interaction between the tip and the prism face. When compared to these extreme cases, the 1 μM AMBI-treated sample (Figure 5b) shows a patchy distribution of the low and high adhesion regions on the nanoprism face. The patches featuring higher adhesion force are assigned to the presence of AMBI.

The appearance of the patches agrees with the partial nucleation of Cu_2O on the prism faces in the initial stage of the shell growth observed in TEM (Figure 4b; 15s). Based on the scanning probe measurements, which characterize the face region of the prism, and the TEM measurements, which are more informative about the prisms' tip/edge regions it can be anticipated that the high surface density molecular patches are directly responsible for blocking specific surface regions of the particles for Cu_2O deposition (**Scheme 1**). During surface treatment, the distribution of AMBI is governed by the local particle surface curvature and the heat treatment process. The former results in a higher local AMBI concentration (especially) at the tips and edges,[15] while the latter promotes the packing of the molecules,[12] resulting in high-density molecular patches. These patches - in contrast to a room temperature treatment where a more uniform distribution of AMBI can be expected - are capable of spatially directing the Cu_2O deposition process by the local modulation of the particles' surface energy. It indicates that in the beginning of the shell deposition, the nucleation and growth of Cu_2O crystallites are effectively prevented at surface sites with high local AMBI concentration, and the Cu_2O shell growth starts at surface sites with lower local AMBI coverage in accordance with earlier results.[7,10] Later into the reaction, the faces of the prisms are effectively covered by Cu_2O, while in the side region, the growing Cu_2O blobs start to merge. The tips, however, are protected during the whole procedure, which points toward a well-defined, high surface coverage and a spatially extended molecular patch in this particle surface region.

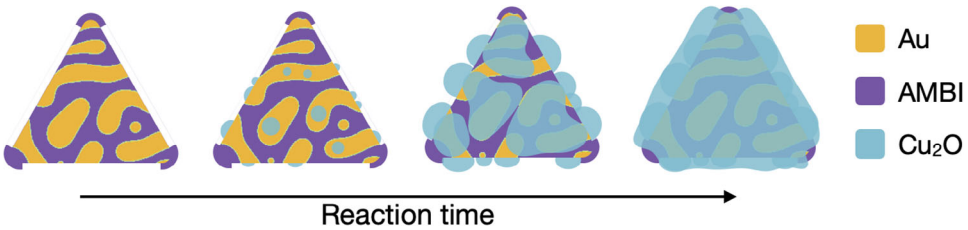

Scheme 1. Anticipated shell growth mechanism based on the transmission electron and scanning probe microscopy measurements.

3. Conclusion

By creating high-density molecular patches on the surface of gold nanoprisms, the spatial control of Cu_2O deposition can be achieved through the nanoscale modification of the surface energy of the particles. Sub-monolayer molecular coverage of the prisms effectively disrupts the otherwise shape-conform Cu_2O shell, and can protect the prisms' tips from the overgrowth. The time-dependent spectroscopic and electron microscopic measurements indicate that for the surface-modified nanoprisms the Cu_2O shell deposition is significantly inhibited in the early stages of the growth process. The shell formation is initiated at well-separated nucleation sites, which spatially extend throughout the process. Nevertheless, the prism tips are protected and remain uncoated, presumably due to the high coverage in this surface region, dictated by curvature and initial ligand density effects.[19] The patchy nature of the molecular coating is also confirmed by conducting scanning probe microscope measurements on individual nanoprisms. Such site-selectively overcoated metal/semiconductor nanoparticles can be of interest for various optoelectronic applications, as the intimate contact between the different phases and the accessibility of the high-intensity plasmonic near-field regions are simultaneously ensured.

4. Experimental Section

Chemicals: The chemical reagents, including hydrogen tetrachloroaurate trihydrate ($HAuCl_4 \bullet 3H_2O$), cetyltrimethylammonium chloride (CTAC, 25 wt.%), ascorbic acid (AA, 99%+), sodium iodide (NaI, 99,5%), sodium borohydride ($NaBH_4$, 99%), sodium dodecyl sulfate (SDS, 99%), copper(II) chloride ($CuCl_2$, 99%), 5-amino-2-mercaptobenzimidazole (AMBI, 96%), sodium hydroxide (NaOH, 98%+), and hydroxylamine hydrochloride ($NH_2OH{\cdot}HCl$, 99,995%+) were purchased from Sigma–Aldrich and used without further purification. All glassware and magnetic stirring bars were thoroughly cleaned using freshly prepared aqua regia (3:1 v/v concentrated HCl:HNO_3), rinsed multiple times with ultrapure water, and dried at 70 °C overnight prior to use. Moisture- and air-sensitive reagents, including $NaBH_4$, NaI, $NH_2OH{\cdot}HCl$, and 5-amino-2-mercaptobenzimidazole (AMBI), were stored in a nitrogen-filled glovebox, and their aqueous solutions were prepared immediately before each synthesis to ensure maximum reactivity and reproducibility. For all experiments, ultrapure water (0.055 µS cm^{-1}) from a Sartorius Arium Mini Plus system was used.

Synthetic Procedures: The gold nanoprisms used in this work were prepared and purified based on CTAC-induced depletion interaction according to an already published literature protocol.[29] The surface modification with 5-amino-2-mercaptobenzimidazole (AMBI) was performed based on published protocols with minor modifications.[7,10] The Au^0 concentration of the purified nanoprism sol was determined based on optical spectroscopy.[30] Then, the concentrations of Au (0) and CTAC were set to 0.315 and 0.22 mM, respectively. Cu_2O shells were deposited based on a published protocol with minor modifications.[20] In a typical synthesis, 2 mL of the above prism sol was added to a magnetically stirred (250 rpm) mixture of SDS (7.475 mL; 0.0464 M) and $CuCl_2$ (15 µL; 0.1 M) in a 22 mL glass vial. Then NaOH was added (250 µL; 1 M) and the stirring was increased to 500 rpm. Hydroxylamine (350 uL; 0.1 M) was quickly injected as a reducing agent to initiate the Cu_2O shell growth, and the stirring was reduced. The shell growth was allowed to proceed for 30 min, and the particles were cleaned through four rounds of centrifugation (3500 rcf, 10 min), changing the dispersion medium to absolute EtOH.

AMBI surface-modified particles were prepared by adding various amounts of AMBI dissolved in EtOH to 200 µL gold prism sample (with the aforementioned Au^0 and CTAC concentrations) and incubated at 60 °C for 2 h in a water bath installed on a heating block (Velp). Thereafter, Cu_2O shell growth was carried out as written above, but scaled down by a factor of 10. This scaled-down synthesis was also used to monitor the surface modification and shell growth over time in situ spectroscopically.

Methods: Standard optical spectra were recorded using a Shimadzu UV-3600i Plus spectrometer. The time-dependent spectra were obtained with a fiber-coupled spectrometer (Thorlabs CCS200) and a stabilized tungsten-halogen light source (Thorlabs SLS201) in a cuvette holder (Thorlabs CVH100). For measurements at elevated temperature, the spectrometer optics was mounted in an optical U-bench (Thorlabs CBB1/M) and placed on a magnetic stirrer hotplate equipped with a temperature probe (Velp). A large optical cuvette (3 × 2 × 3 cm) was placed in the U-bench, which functioned as the thermostating water bath and accommodated the semi-micro cuvette with the actual sample. In the custom control software written in LabView, 2.5 ms integration time was used with 100 averages. In the first few minutes of the measurement, spectra were recorded every second, after which sampling was performed less frequently. The measured spectra were batch-processed using OriginPro. Both AMBI adsorption and Cu_2O shell growth were monitored in the setup. The shell growth was also quenched at different time instances to obtain the time-dependent morphology of the particles. 10 µL of the sample was withdrawn from the growth solution and quickly injected into 1 mL EtOH. The sample was washed with EtOH and concentrated by repeated centrifugation (3500 rcf; 15 min). For ex situ scanning and transmission electron microscopy, 1.5 µL of the cleaned samples was drop-cast on a silicon wafer or carbon-coated TEM grids (Ted Pella), respectively. SEM images were recorded on a Zeiss LEO 1540-XB instrument at 5 keV, and TEM images were obtained with a JEOL 3010 operated at 300 keV. Scanning probe measurements were carried out in PeakForce tapping mode using a MultiMode 8 instrument from Bruker. In this mode, a complete force-distance curve was measured at every position, and the topographic data were recorded at the maximum force set between the sample and the cantilever. This maximum force was set to 1 nN. The adhesion force data were extracted by the controller software in real time, providing adhesion maps that have the same resolution as the corresponding topographic images. For these measurements, ScanAsyst-Air cantilevers (Bruker) with a nominal tip radius of R = 2 nm and spring constant of k = 0.4 N m^{-1} were used. For the measurements, ITO slides (PGO GmbH) were cleaned by ultrasonication (15 min in acetone, 15 min in 2-propanol, 15 min in water, 1 min air plasma treatment), and the particles were spin-coated at 3000 rpm, then extensively rinsed with absolute ethanol.

Supporting Information

Supporting Information is available from the Wiley Online Library or from the author.

Acknowledgements

D.K. acknowledges the support of Pro Progressio and the József Varga Foundation. The work was financially supported by the NRDI Fund of Hungary under the grant OTKA FK 142148. Project no. TKP2021-NKTA-05 has been implemented with the support provided by the Ministry of Innovation and Technology of Hungary from the National Research, Development and Innovation Fund (NRDI), financed under the TKP2021 funding scheme. Z.O. acknowledges the financial support from the National Research, Development and Innovation Office (NKFIH) in Hungary, through the Grant No. K-134258. Funding: National Research, Development and Innovation Fund (NRDI) FK-142148, TKP2021-NKTA-05, K-134258.

Conflict of Interest

The authors declare no conflict of interest.

Data Availability Statement

The data that support the findings of this study are available in the supplementary material of this article.

Keywords

colloidal systems, heterostructures, nanoparticles, surface patterning

Received: June 6, 2025
Revised: July 3, 2025
Published online: July 31, 2025

[1] M. Volokh, T. Mokari, *Nanoscale Adv.* **2020**, *2*, 930.
[2] Y. Q. Wang, K. Nikitin, D. W. McComb, *Chem. Phys. Lett.* **2008**, *456*, 202.
[3] C.-H. Kuo, T.-E. Hua, M. H. Huang, *J. Am. Chem. Soc.* **2009**, *131*, 17871.
[4] D. Kovács, A. Deák, G. Z. Radnóczi, Z. E. Horváth, A. Sulyok, R. Schiller, O. Czömpöly, D. Zámbó, *J. Mater. Chem. C* **2023**, *11*, 8796.
[5] M. H. Huang, S. Rej, C. Chiu, *Small* **2015**, *11*, 2716.
[6] J. Zhu, N. Lu, W. Chen, L. Kong, Y. Yang, D. Ma, S. Huang, *J. Nanomater.* **2015**, *2015*, 389790.
[7] W. Xu, J. Jia, T. Wang, C. Li, B. He, J. Zong, Y. Wang, H. J. Fan, H. Xu, Y. Feng, H. Chen, *Angew. Chem. Int. Ed.* **2020**, *59*, 22246.
[8] Y. Wang, M. Zheng, S. Liu, Z. Wang, *Nanoscale Res. Lett.* **2016**, *11*, 390.
[9] E. D. R. Legaspi, M. D. Regulacio, L. A. E. Pineda, L. V. A. Sayson, W. Jiang, J. Z. X. Heng, W. Wu, E. Ye, *ChemistrySelect* **2023**, *8*, 202300904.
[10] W. Xu, R. Xiao, S. An, C. Li, J. Ding, H. Chen, H. B. Yang, Y. Feng, *Small* **2023**, *19*, 2300587.
[11] J. Redolat, M. Camarena-Pérez, A. Griol, M. S. Lozano, M. I. Gómez-Gómez, J. E. Vázquez-Lozano, E. Miele, J. J. Baumberg, A. Martínez, E. Pinilla-Cienfuegos, *Nano Lett.* **2024**, *24*, 3670.
[12] Y. Feng, J. He, H. Wang, Y. Y. Tay, H. Sun, L. Zhu, H. Chen, *J. Am. Chem. Soc.* **2012**, *134*, 2004.
[13] Y. Wang, J. Jia, J. Zhang, R. Xiao, W. Xu, Y. Feng, *Small* **2023**, *19*, 2207907.
[14] T. Jiang, J. Zong, Y. Feng, H. Chen, **2023**, *1*, 94.
[15] Z. Wang, Y. Zhou, J. Wang, Y. Wang, J. Zhao, W. Xu, Y. Feng, *ACS Appl. Nano Mater.* **2024**, *7*, 22002.
[16] Y. Feng, Y. Wang, X. Song, S. Xing, H. Chen, *Chem. Sci.* **2017**, *8*, 430.
[17] J. Jia, G. Liu, W. Xu, X. Tian, S. Li, F. Han, Y. Feng, X. Dong, H. Chen, *Angew. Chem. Int. Ed.* **2020**, *59*, 14443.
[18] A. Kim, S. Zhou, L. Yao, S. Ni, B. Luo, C. E. Sing, Q. Chen, *J. Am. Chem. Soc.* **2019**, *141*, 11796.
[19] K. N. L. Hoang, S. M. McClain, S. M. Meyer, C. A. Jalomo, N. B. Forney, C. J. Murphy, *Chem. Commun.* **2022**, *58*, 9728.
[20] D. Zámbó, D. Kovács, A. Deák, *Part & Part Syst Charact* **2024**, *41*, 2400082.
[21] E. Vernack, D. Costa, P. Tingaut, P. Marcus, *Corros. Sci.* **2020**, *174*, 108840.
[22] Y. Shang, L. Guo, *Adv. Sci.* **2015**, *2*, 1500140.
[23] S. Hussain, S. Karim, Y. Pang, *ChemistrySelect* **2024**, *9*, 202400884.
[24] S. Pothorszky, D. Zámbó, T. Deák, A. Deák, *Nanoscale* **2016**, *8*, 3523.
[25] P. M. R. Paulo, P. Zijlstra, M. Orrit, E. Garcia-Fernandez, T. C. S. Pace, A. S. Viana, S. M. B. Costa, *Langmuir* **2017**, *33*, 6503.
[26] V. Myroshnychenko, N. Nishio, F. J. García de Abajo, J. Förstner, N. Yamamoto, *ACS Nano.* **2018**, *12*, 8436.
[27] D. P. Szekrényes, D. Kovács, Z. Zolnai, A. Deák, *J. Phys. Chem. C* **2020**, *124*, 19736.
[28] J. C. Love, L. A. Estroff, J. K. Kriebel, R. G. Nuzzo, G. M. Whitesides, *Chem. Rev.* **2005**, *105*, 1103.
[29] L. Scarabelli, L. M. Liz-Marzán, *ACS Nano* **2021**, *15*, 18600.
[30] N. G. Khlebtsov, B. N. Khlebtsov, E. V. Kryuchkova, S. V. Zarkov, A. M. Burov, *J. Phys. Chem. C* **2022**, *126*, 19268.